ACI STRUCTURAL JOURNAL TECHNICAL PAPER

Title no. 93-S28

Analysis of Reinforced Concrete Members Subject to Shear and Axial Compression



by Robert G. Selby, Frank J. Vecchio, and Michael P. Collins

The recent catastrophic failure of an offshore platform brought back into question the shear design of reinforced concrete members. Specifically, there is renewed suspicion that the current design practice may be unconservative for members without shear reinforcement when such members are subjected to shear and axial compression. This paper describes nonlinear finite element analyses made to determine the shear response of the tri-cell regions of two offshore structures; regions subjected to such loading conditions. The accuracy of the finite element procedure is demonstrated by comparing its predictions with the experimental response of a series of specimens tested under varying ratios of shear-to-axial compression. It is concluded that, while current empirical code equations do not perform adequately under the conditions considered, nonlinear analyses can provide reliable results.

Keywords: compression; concretes; shear properties; structural design; tests.

INTRODUCTION

Elements of reinforced concrete offshore platforms have typically been designed for shear and axial compression using design rules that were derived over 30 years ago from tests performed on under-reinforced, normal-strength concrete beams.[1] The current ACI code[2] and earlier editions of the Norwegian standard NS3473[3] both adopted design equations based on such data for members without shear reinforcement. However, the failure of the Sleipner A Gravity Base Structure in 1991 has brought this design practice back into question. Gupta and Collins[4] have since shown that current design equations are unconservative and routinely overestimate the beneficial effects of axial compression on the shear strength.

This paper demonstrates the ability of nonlinear finite element analyses to accurately capture the behavior of reinforced concrete elements, with and without shear reinforcement, subjected to varying ratios of shear and axial compression. The finite element results are compared to experimental results and to predictions from the ACI code. Analyses of shear critical regions of two offshore structures also indicate the inadequacy of the current practice and demonstrate the need for the adoption of rational models for predicting shear behavior.

RESEARCH SIGNIFICANCE

Many modern structures, particularly offshore structures, contain elements subjected to high levels of axial compression and shear. It has been shown elsewhere that current design code specifications for such elements may be highly unconservative. This paper shows that finite element analyses can provide accurate estimates of behavior, load capacity, and failure mode in such cases.

FINITE ELEMENT MODEL

The finite element program SPARCS was developed[5,6] to enable compression field analysis of reinforced concrete solids. The constitutive relationships used were derived from the modified compression field theory.[7] A relatively simple approach was taken with the finite elements and solution techniques that were employed.

Relatively low-powered eight-noded brick, six-noded wedge, and two-noded truss elements (Fig. 1) were formulated in such a way that costly numerical integration procedures were avoided. The element stiffness matrix for each element was evaluated explicitly and results were built into the computer program. These finite elements, based on linear displacement functions, are able to adequately represent discontinuous stress fields.[8] Note that small displacements and infinitesimal rotations were assumed in the derivation of the element stiffness matrix. As well, stresses, strains, and material properties were considered uniform throughout an element.

The analysis algorithm used is based on an iterative linear elastic formulation in which secant moduli are defined and progressively refined according to current local total stress-strain states. An analysis begins by assuming linear elastic isotropic material properties. Element stiffness matrices are

ACI Structural Journal, V. 93, No. 3, May-June 1996.

Received July 26, 1994, and reviewed under Institute publication policies. Copyright © 1996, American Concrete Institute. All rights reserved, including the making of copies unless permission is obtained from the copyright proprietors. Pertinent discussion will be published in the March-April 1997 *ACI Structural Journal* if received by Nov. 1, 1996.

ACI member ***Robert G. Selby*** *is a research engineer with Morrison Hershfield Ltd. of Toronto. He received his BSc degree from the University of Alberta in 1988 and his PhD from the University of Toronto in 1993. His research interests include nonlinear analysis and constitutive modeling of reinforced concrete structures.*

ACI member ***Frank J. Vecchio*** *is a professor of civil engineering at the University of Toronto. He is a member of ACI Committees 441, Columns, and 447, Finite Element Analysis. His research interests include constitutive modeling, nonlinear analysis, and computer-aided design of reinforced concrete.*

Michael P. Collins*, FACI, is a professor of civil engineering at the University of Toronto. He is a member of joint ACI-ASCE Committee 445, Shear and Torsion, and has served as chairman of the Canadian Standards Association Committee on Concrete Offshore Structures.*

calculated, the global stiffness is assembled, and the load vector is formed. Nodal displacements are determined, from which one strain tensor is calculated for each element. Principal strains and corresponding directions are then found. The concrete and steel stresses are evaluated using the constitutive models, permitting determination of secant moduli and, in turn, new material stiffness matrices. Average secant moduli are calculated and, if they have converged to the specified limit, then the analysis is complete. Otherwise, the newly calculated material stiffness values are used to perform another linear elastic analysis. Normally, satisfactory convergence is achieved within 10 to 30 iterations.

The material models implemented are based on the constitutive relationships of the modified compression field theory that were developed from cracked reinforced concrete panels tested under plane stress conditions.[7] The constitutive model treats concrete as an orthotropic material with equilibrium, compatibility, and stress-strain relationships satisfied in terms of average stresses and strains. The directions of the principal stresses and strains are assumed to coincide. To adequately describe the response of reinforced concrete, models are included for strength degradation due to cracking, strength enhancement due to confinement, pre- and postpeak stress-strain response in tension and compression, concrete lateral expansion, and crack slip.

The constitutive equations for multiaxial stress states are based on modifications to the concrete uniaxial stress-strain curve. The uniaxial stress-strain response of normal-strength concrete is modeled with an equation whose shape is tuned to the concrete cylinder strength. It resembles a parabola for normal-strength concrete, but for high-strength concrete it has a more linear ascending branch and a more sharply declining descending branch (Fig. 2).

Lateral confining stresses increase the strength, stiffness, and ductility of concrete. Strength enhancement is modeled by modifying the peak stress of the base curve [Fig. 3(a)]. A four-parameter failure surface[9] is used to find the concrete strength under confining stresses. The SPARCS model recognizes that the peak strain increases more rapidly than the peak stress under multiaxial compressive stresses, and the postpeak ductility is improved under confining stresses. The increased lateral straining that concrete exhibits near ultimate is modeled by using variable Poisson's ratios in the orthotropic model [Fig. 3(b)].

In stress states involving tension, large tensile strains perpendicular to the principal compressive direction reduce the

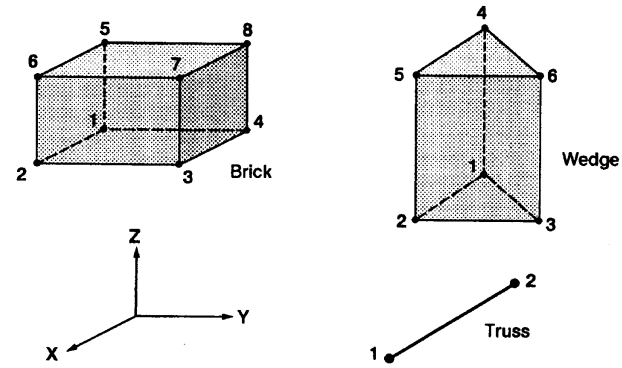

Fig. 1—SPARCS element library

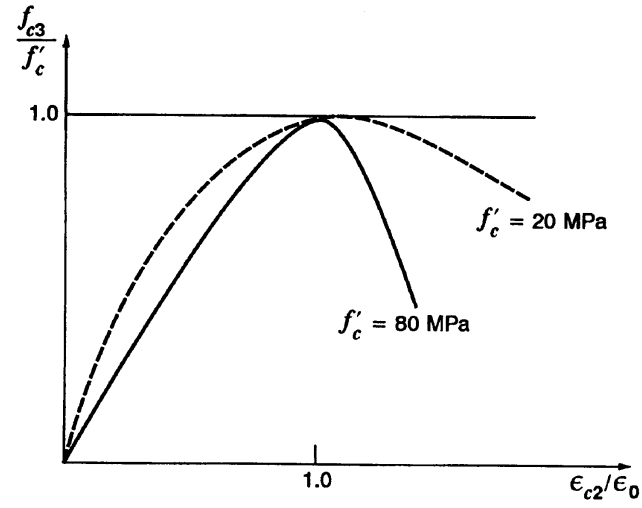

Fig. 2—Compressive stress-strain base curve

concrete compressive strength [Fig. 3(b)]. This compression softening effect is modeled by making the concrete compressive stress f_{c3} a function of both the compressive principal strain ε_{c3} and the tensile principal strain ε_{c1}. A linear tensile stress-strain relationship is used until the concrete tensile principal stress f_{c1} reaches the concrete tensile strength. Due to the influence of bond, tensile stresses can develop in the concrete between cracks. A descending branch in the post-cracked region accounts for this tension stiffening effect [Fig. 3(b)].

Although the constitutive model is cast in terms of average stresses and strains, local conditions at cracks are considered. The presence of average tensile stresses in the concrete implies that local stress in the reinforcement increases at crack locations to carry the average tensile stresses across the crack. Thus, local conditions must be checked to insure that the concrete tensile stress can be transmitted across the crack. The local reinforcement stresses at a crack must not violate the yield condition; otherwise the tensile principal stress f_{c1} must be reduced accordingly.

The local increases in the reinforcement stresses may, in turn, require shear stresses on the crack surfaces for equilibrium. As the crack widths increase, the ability of the concrete

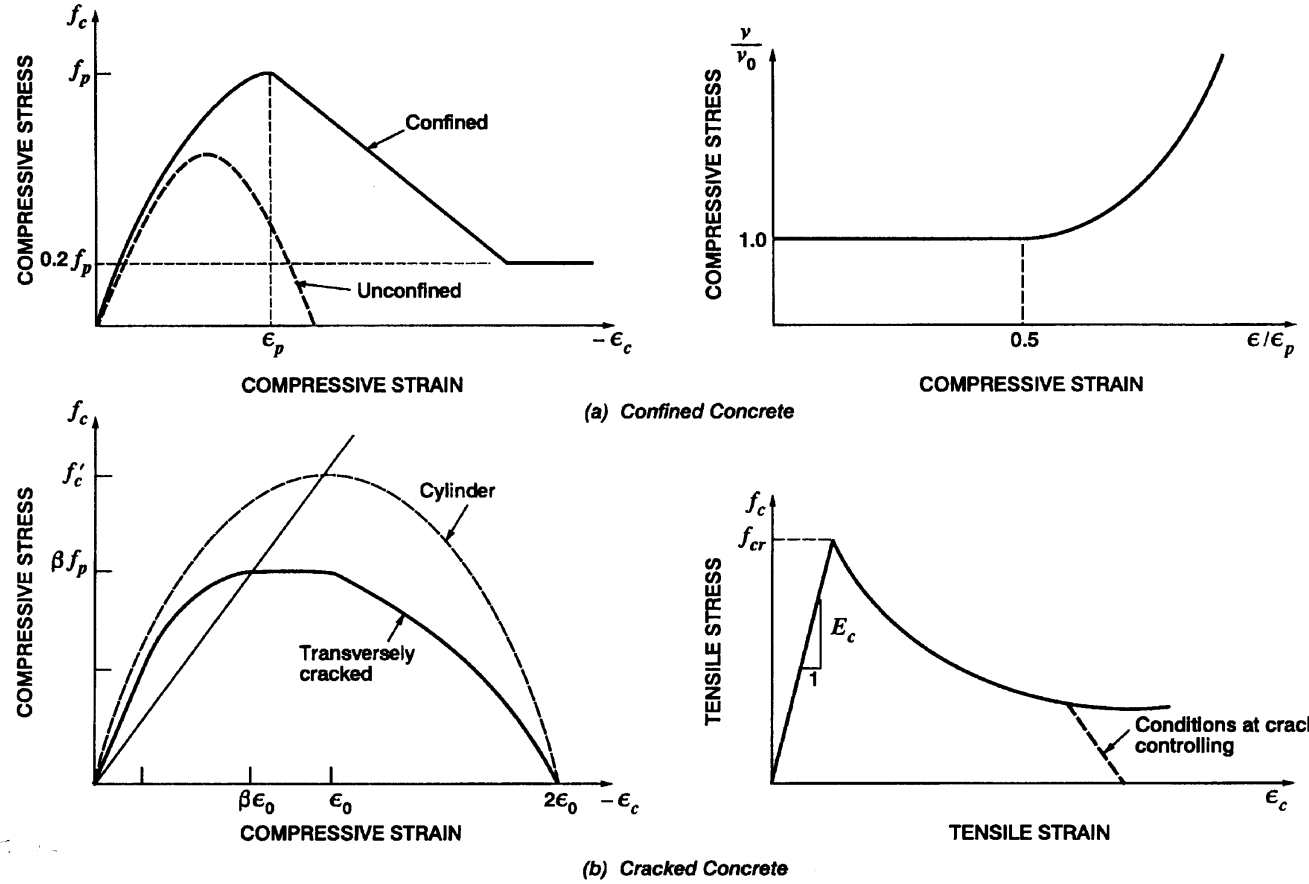

Fig. 3—Concrete constitutive models: (a) confined concrete; (b) cracked concrete

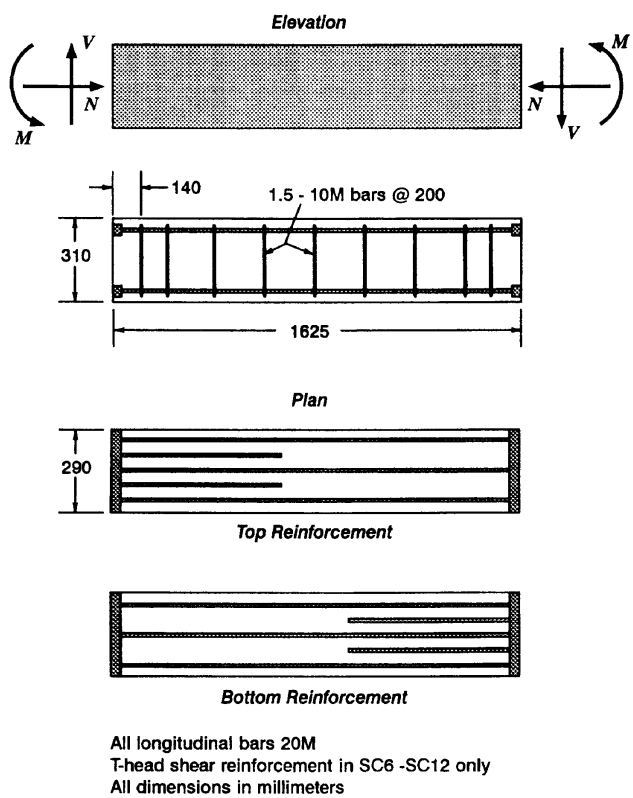

Fig. 4—Details of SC beams

to transmit shear by aggregate interlock decreases. This may inhibit the local stress increases in the reinforcement and, in turn, limit the average concrete tensile stress. Crack slip is said to occur if the required shear stresses cannot be supported at higher crack widths. Further details regarding the finite element formulation and constitutive modeling are given by Selby and Vecchio.[10]

EXPERIMENTAL CORROBORATION

A series of beams was tested by Gupta and Collins[4] to gain insight into the behavior of reinforced concrete elements subjected to high compression and shear typical of offshore structures. The beam strips were 310-mm-(12.2-in.)-deep, 290-mm-(11.4-in.)-wide, and 1625-mm-(64.0-in.)-long. Three 20M bars on both the top and bottom faces, with a cover of 32 mm (1.25 in.), were used for the longitudinal reinforcement. An additional two 600-mm-(24-in.)-long 20M bars were provided on the tension faces of the beam (Fig. 4). Specimens SC1 through SC5 contained no shear reinforcement. T-headed stirrups were used in Specimens SC6 through SC12, and stirrups with standard 90 deg bends were used in Specimens SC13 to SC15. Shear reinforcement consisted of 10M bars in a staggered pattern resulting in an out-of-plane reinforcement ratio of 0.26 percent. The beams were constructed of high-strength concrete with a cylinder strength of about 60 MPa [8.7 ksi (Table 1)]. The strain at peak stress from the cylinder tests was 0.0023 mm/mm. The

Table 1—Gupta/Collins[4] test beams

Specimen	N/V	f'_c, MPa	V_{test}, kN	Failure mode	V_{sp}, kN	Predicted mode	Test/ SPARCS
SC1	4:1	60.9	238	D, S	242.5	S	0.981
SC2	8:1	60.9	205	D	277.5	D	0.739
SC3	0:1	60.9	118	S	150.0	S, F	0.787
SC4	64:1	60.9	59	C	61.0	C, YC	0.967
SC5	14:1	60.9	260	C, D	200.0	C, YC	1.300
SC6	64:1	62.4	77	C	76.0	C, YC, YZ	1.013
SC7	0:1	62.4	240	S, F	200.0	S, F, YZ	1.200
SC8	4:1	62.4	385	S	400.0	S, F, YZ	0.963
SC9	8:1	62.4	392	S	365.0	S, YC, YZ	1.074
SC11	14:1	60.2	265	S	260.0	C, YC	1.019
SC12	6:1	60.2	405	S	385.0	S, YC, YZ	1.052
						Mean =	1.008

Note:
D = diagonal cleavage failure.
S = shear failure.
YC = yield of compression steel.
F = flexural failure.
C = compression failure.
YZ = yield of T-heads.

longitudinal reinforcement had a yield strength of 387 MPa (56 ksi) and the shear reinforcement had a yield strength of 452 MPa (65.5 ksi). The modulus of elasticity of the steel was assumed to be 200,000 MPa (29,000 ksi).

The current ACI 318-89 code provisions have been reported[4] as being especially unconservative for beams containing no shear reinforcement, while code predictions for elements with stirrups were less unconservative. Even small amounts of shear reinforcement were found to increase the strength considerably. The beneficial effect of the shear reinforcement increased with higher axial compression due to the restraint provided to the longitudinal bars. Specimens without shear reinforcement typically failed by formation of a single diagonal crack running from end to end. Specimens containing shear reinforcement failed after several diagonal cracks had formed.

For finite element analysis of the test specimens, a mesh of 480 brick elements was formulated [Fig. 5(a)]. Twelve elements were used through the depth of the beam, and the left end of the mesh was restrained in the axial and transverse directions. Nodal loads were applied at the right end of the mesh, corresponding to the appropriate shear, moment, and axial load. A smeared steel representation was used to model all reinforcement, using the five material zones identified in Fig. 5(b). Elements at both ends of the beam were given stiff properties to facilitate load transfer. An elastic perfectly-plastic steel model was used. A crack spacing of 220 mm [8.7 in. (i.e., the spacing of the longitudinal bars)] was assumed.

The results of the SPARCS analyses are presented in Table 1. The experimental-to-theoretical ratio for the ultimate load capacity for 11 specimens was 1.008, with an acceptable coefficient of variation of 15.8 percent. The results are also shown in Fig. 6(a) in a shear force-axial load interaction diagram. The analytical curves follow the experimental trends rather well. Initially, the applied axial force significantly enhanced the load-carrying capacity, but it then had progressively less influence. Eventually, the axial load

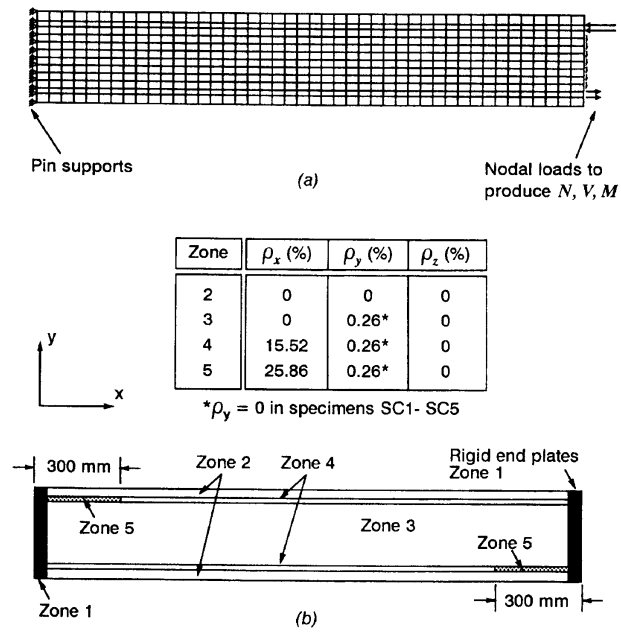

Fig. 5—Finite element model for SC beams: (a) mesh; (b) material modeling

had a detrimental effect on the ultimate strength. The plot clearly shows the substantial increase in strength, for all ratios of axial compression to shear, realized with a modest amount of shear reinforcement. For each of the specimens without shear reinforcement, a brittle failure mechanism was determined. By adding the shear reinforcement, the failure mechanism became more ductile, with the exception of Specimen SC6 ($N/V = 64$).

Specimens subjected to the highest axial compression were observed to fail by crushing of the concrete. Failure of Specimen SC4 included buckling of the longitudinal bars. The companion to this specimen (SC6) failed at a higher load since the T-headed bars restrained the longitudinal reinforcement. The theoretical model cannot predict buckling of rein-

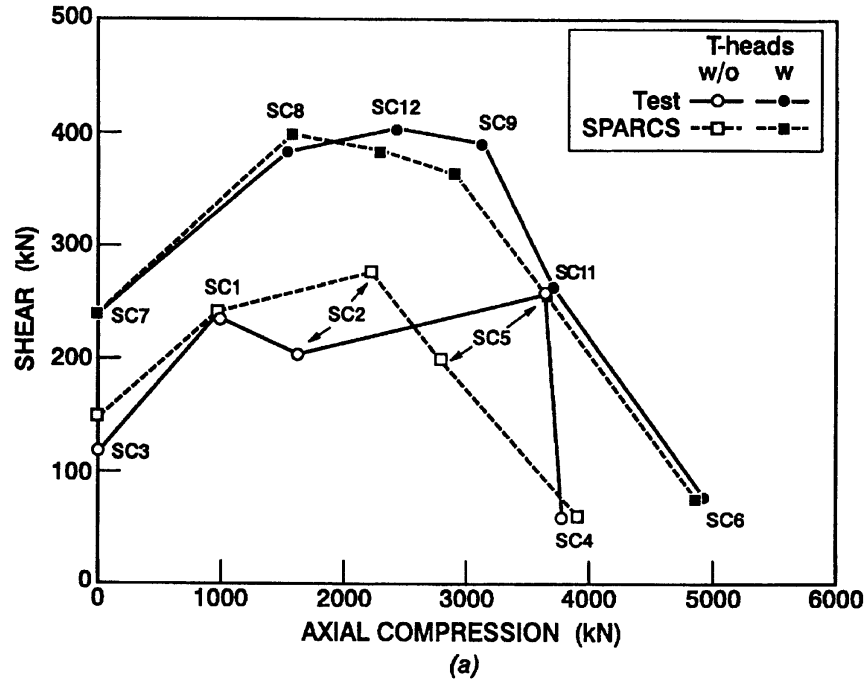

(a)

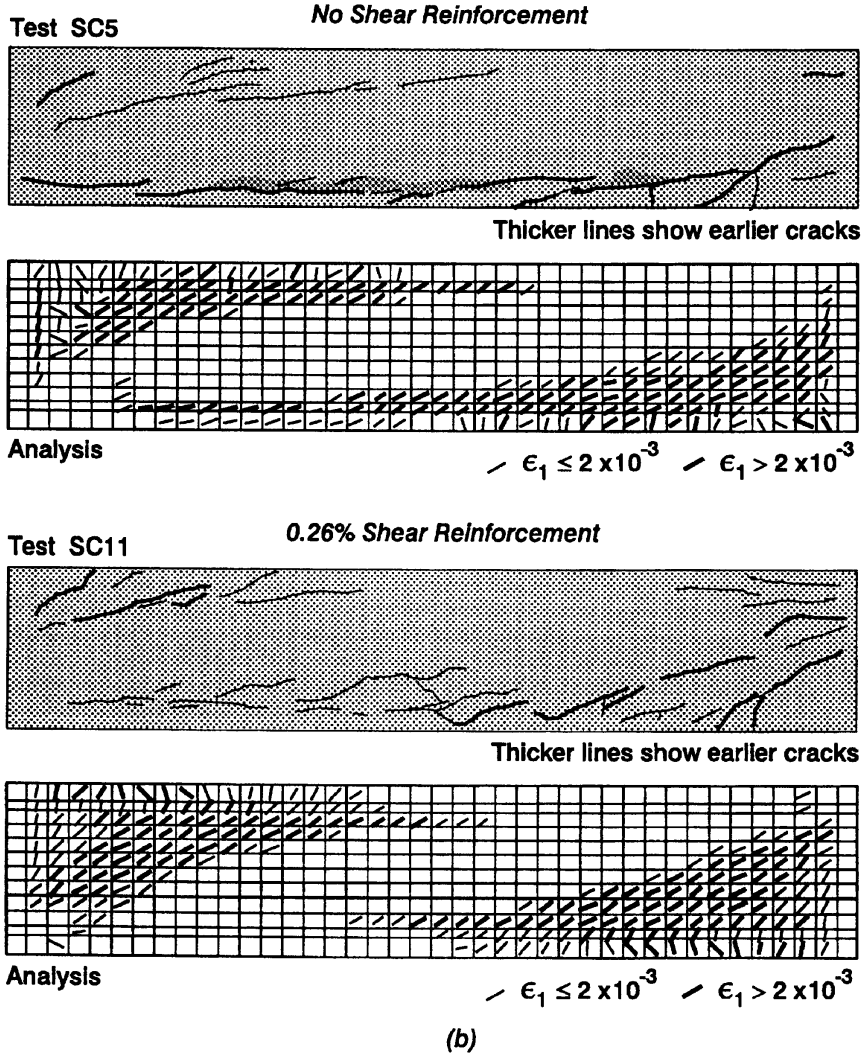

(b)

Fig. 6—Analysis results for SC beams: (a) shear/axial force interaction diagram; (b) comparison of crack patterns at ultimate, N/V = 4

forcement, so this failure mechanism was not identified. The theoretically determined failure of SC4 was due to crushing of the concrete in the elements near the ends of the beam. This failure was somewhat premature due to the manner in which the loads were introduced. The high compressive forces were concentrated at the level of the longitudinal reinforcement causing the local crushing. A simple sectional analysis of the specimen would produce a compression failure at a load about 25 percent higher than the SPARCS analysis. The distribution of the applied nodal forces could be changed to alleviate this problem. However, in an attempt to obtain "predictions," the modeling decisions were made for all specimens before any analyses were performed and each specimen was analyzed only once. The model found a higher failure load for Specimen SC6 because of the confinement provided by the shear reinforcement.

Specimens loaded at an axial force-to-shear force ratio of 14 (i.e., SC5 and SC11) experienced brittle failures at almost the same load. SC5 was reported to have failed due to crushing and diagonal cleavage. SC11 failed due to formation of a single diagonal crack. SPARCS determined a crushing failure for both specimens, with little cracking before failure. Specimens without shear reinforcement and subjected to moderate levels of axial compression (i.e., SC1 and SC2) failed by the formation of a single shear crack. These brittle mechanisms were reproduced by the finite element model. Flexural cracking was observed in the numerical analyses for both specimens at fairly low levels of applied shear force [about 40 and 60 kN (9.0 and 13.5 kip), respectively]. Failure occurred before any reinforcement was predicted to yield. Adding the shear reinforcement to these specimens (i.e., SC8, SC9, SC12) resulted in several diagonal cracks being formed before shear failure. This behavior was also evident in the analytical model [Fig. 6(b)]. The calculated load history typically involved flexural shear cracking, followed by yielding of the stirrups near the cutoff points, then shear-compression failure of the concrete diagonals.

The analytical model displayed the correct failure modes for the specimens loaded without axial compression. The model without shear reinforcement (i.e., SC3) experienced a shear failure, but at a load about 25 percent higher than the experimental value. Much more cracking was determined for this specimen and the longitudinal steel was found to yield at the bar cutoff points. After inclined cracks first appeared, the model seemed to carry the shear by direct strut action. The T-headed reinforcement doubled the strength of the specimen and changed the mechanism to one of a shear failure combined with yielding of the longitudinal reinforcement. This behavior was reproduced by SPARCS. Deformations in the specimens were well-duplicated by the numerical analyses. The tangential deviation of the specimens was measured to give an indication of the total deflection (the tangential deviation was defined as the displacement along a line perpendicular to tangents to each end of the beam; since the left end of the finite element mesh was fixed, the tangential deviation of the model was the deflection of the right end of the beam). Typical measured and calculated values are compared in Fig. 7(a). The stiffness of the specimens increased as the axial compressive force was increased. The presence of shear reinforcement had little effect on the initial stiffness, but it

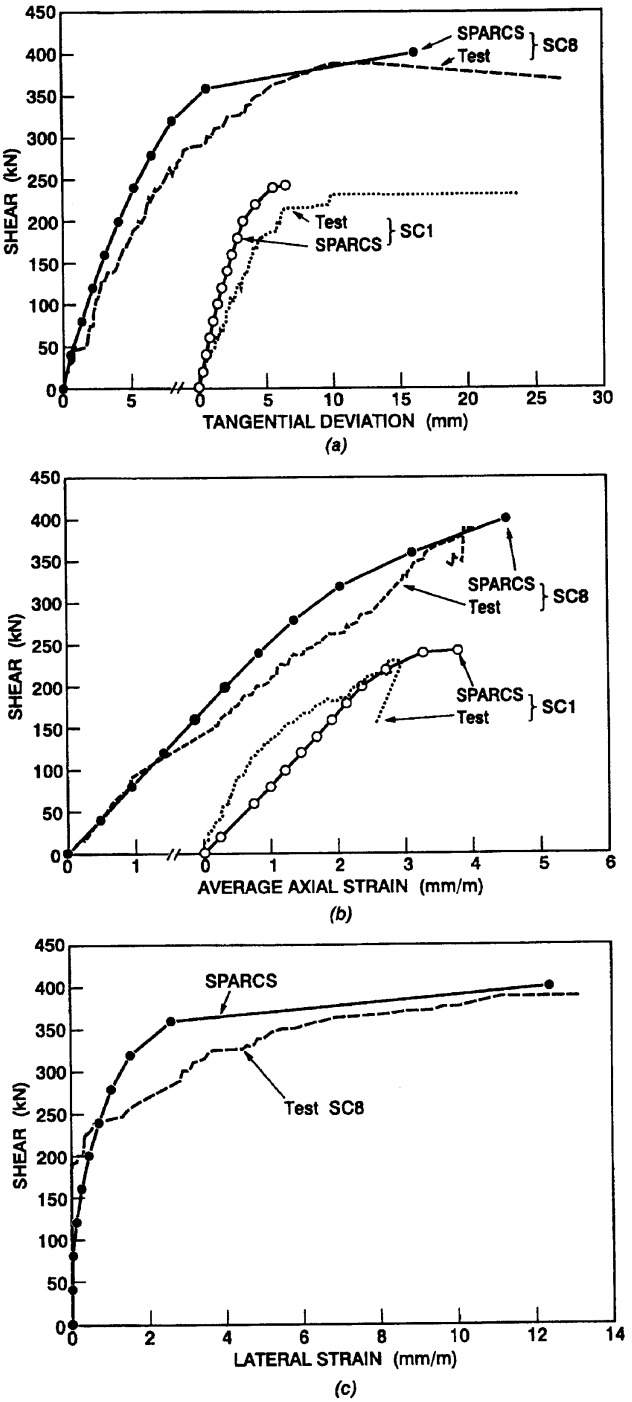

Fig. 7—Analysis results for SC beams: (a) comparison of tangential deviation, N/V = 4; (b) comparison of average axial strains, N/V = 4; (c) comparison of lateral strains, N/V = 4

did have a significant effect on the strength. Other measures of deformation were also in good agreement with the experimentally observed response, including average axial strain at mid-depth [Fig. 7(b)], reinforcement strains, and lateral strains [Fig. 7(c)]. The analytical axial strains were calculated from the nodal displacements at the beam midheight over the same gage length as that used in the tests. The experimental axial strains were measured with a linear variable differential transformer (LVDT) mounted at midheight on each side of the beam. In a similar manner, lateral strains were cal-

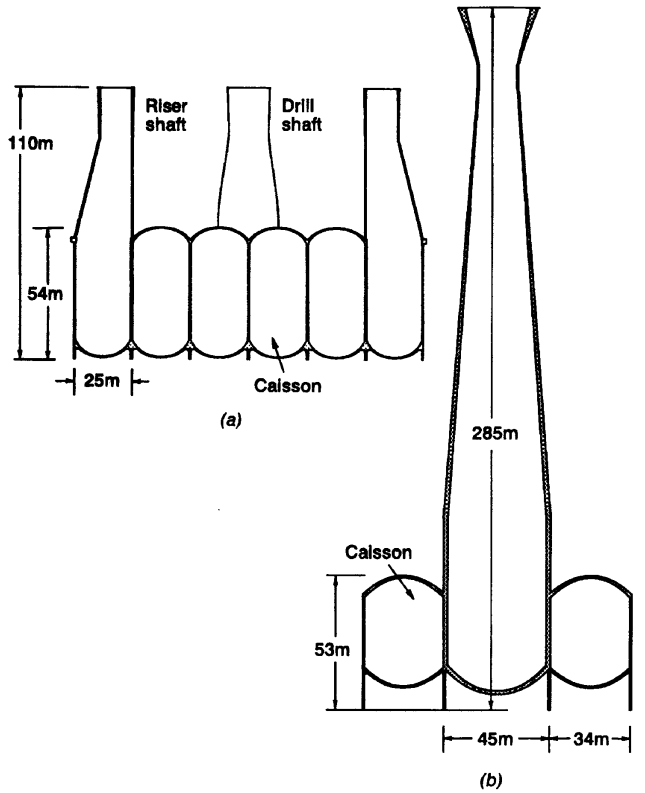

Fig. 8—Offshore platforms: (a) Sleipner A GBS; (b) Draugen GBS

culated from the nodal displacements and compared with the appropriate LVDT readings.

The SPARCS analyses were able to quantify the beneficial effects of the shear reinforcement. Generally, successful modeling of the specimens without shear reinforcement, which failed in brittle modes, involved identifying the onset of inclined cracking. The compression softening model was crucial in modeling the ductile behavior of specimens that contained shear reinforcement. No doubt the inclusion of Poisson's effect in cracked concrete also had some influence on the computed response, especially for Specimens SC8, SC9, and SC12, which failed in shear and were subjected to appreciable levels of axial compression.

APPLICATION TO OFFSHORE STRUCTURES

The SPARCS program was used to perform highly detailed, local, nonlinear finite element studies of critical regions of offshore structures subjected to high axial compression and out-of-plane shear. The investigations provided considerable information regarding stresses, deformations, and failure mechanisms. Two such analyses are discussed below.

The Sleipner A Gravity Base Structure (GBS) was an offshore platform planned for gas drilling operations in the North Sea. The structural system employed a conventional gravity base form. The structure was 110-m-(361-ft.)-high and was comprised of skirts and lower domes to form the bottom—20 25-m-(82-ft.)-diameter caissons for ballast and storage and four full-height tapered shafts [Fig. 8(a)]. Thirty-two tricells were formed at the intersections of the cylindrical shafts and caissons. The shaft and caisson walls were 500-mm-(19.7-in.)-thick, except in the tricell region; the tricell wall was 550-mm-(21.7-in.)-thick, the common wall was 800-mm-(31.5-in.)-thick, and the inner part of the tricell wall spanned 4.378 m (14.4 ft). Since water freely passed into this region due to an opening at the top of the tricell, a net hydrostatic pressure acted across the tricell wall.

In August 1991, failure of the Sleipner platform occurred during the preparation for the deck-mating operation (this procedure involves flooding the caissons to submerge the structure so that just a small part of the shafts extend above the water line. Barges then bring the production facilities in place over the concrete base. After the two structures are connected, the gravity base is deballasted, raised, and towed to the drilling site). The caissons were being filled to allow Sleipner to descend at a controlled rate of about 3 m/hr (9.8 ft/hr). When the structure reached a depth of 99 m (325 ft), a loud rumbling noise was heard from one of the structure's two drill shafts. Water began rushing into Drill Shaft D3 faster than it could be pumped out, causing Sleipner to sink at a rate of about 1 m/min (3.28 ft/min). The structure was abandoned and it imploded soon after disappearing below the water surface. A later survey of the 220-m-(722-ft)-deep fjord revealed that no debris larger than 10 m (33 ft) remained of this enormous structure. The disaster was attributed to a failure of Tricell T23 adjacent to Drill Shaft D3. The failure occurred at an elevation of about 34 m (112 ft), which implied that 65 m (213 ft) of water pressure had been on the tricell wall.

In the vicinity of the tricell failure, the horizontal and vertical reinforcement at each wall face consisted of 25-mm (1.0-in.) bars spaced at 170 mm (6.7 in.) [Fig. 9(a)]. The only other reinforcement provided in the tricell was a single 1-m-(3.3-ft)-long T-headed bar spaced at 170 mm (6.7 in.) vertically. No shear reinforcement was included in the tricell walls at this location, although a small amount was in the lower regions of the structure. Approximately 0.4 percent T-headed reinforcement was used in the shaft tricell walls from the base to an elevation of 20 m (65.6 ft), where it was cut back to 0.2 percent. At an elevation of 32 m (105 ft), shear reinforcement was discontinued. The concrete used had a cylinder strength of 60 MPa (8.7 ksi). The steel had a yield stress of 550 MPa (79.7 ksi).

A local nonlinear finite element analysis was performed on the Sleipner tricell region to assess its load-carrying capacity. Due to symmetry, modeling one-sixth of a 1-m (3.3-ft) height of the tricell region was adequate. The one-element-thick mesh contained 342 brick elements and 338 wedge elements [Fig. 9(b)]. Additional truss elements were later added to the mesh to vary the length of the T-headed reinforcement. Roller supports were used to model the symmetry conditions at the midspan of the tricell wall and along the center line of the cell wall. Roller supports were also used to restrain the vertical movement of the bottom layer of nodes. The cell wall axial compressive force of 5 MN/m (340 kip/ft) was applied as equivalent nodal loads at the end of the shaft wall. The inner part of the tricell wall was subjected to the net hydrostatic pressure. A vertical compressive stress of 7 MPa (1.01 ksi) was also included. The axial load was held constant while the net hydrostatic pressure was increased to failure.

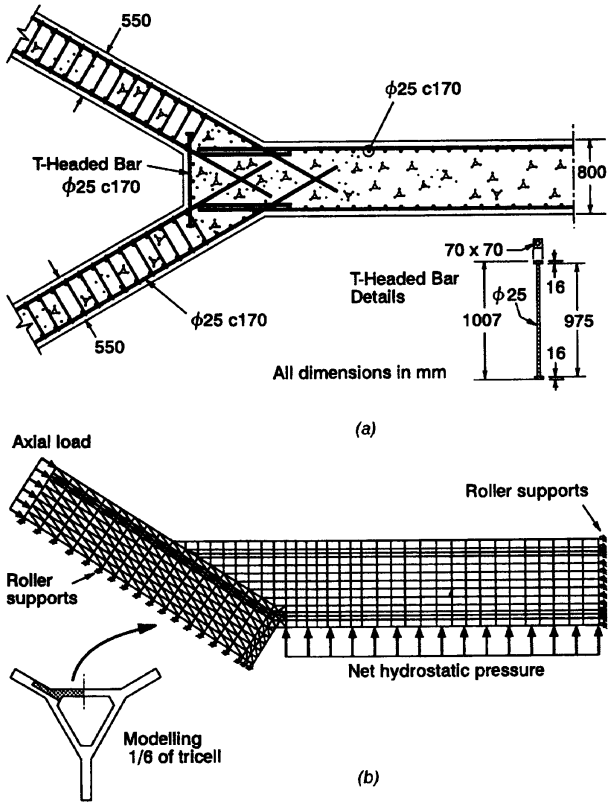

Fig. 9—Sleipner A tricell: (a) reinforcing details; (b) finite element model

The SPARCS model predicted failure at a net hydrostatic pressure of 0.625 MPa (91 psi), which agreed well with the observed failure at an estimated pressure of 0.65 MPa (94 psi). The model indicated a shear failure occurred just around the end of the terminated T-headed bar. Apparently, the bar was not long enough. If it had been 1.5-m-(4.9-ft)-long, instead of 1.0-m-(3.3-ft)-long, studies indicated that the design would have worked. Of interest is the fact that the ACI code equations predicted an ultimate pressure over twice that acting at failure [1.45 MPa (210 psi)] versus 0.65 MPa (94 psi). While a nonlinear finite element analysis is not appropriate for routine design, a simple, sectional analysis, also based on the modified compression field theory, quickly produced a prediction of 0.45 MPa (65 psi). Further details of the failed structure and the analysis results are discussed by Collins et al.[11]

In light of the Sleipner accident, the adequacy of the Draugen GBS tricell region required verification. Draugen is an offshore structure that was under construction at the time of the Sleipner accident. Analyses were undertaken with the SPARCS program to determine the performance of the tricell during the deck-mating. Also, the ultimate strength and failure mode of the tricell were sought.

The Draugen platform [Fig. 8(a)] consists of a single 276-m-(905-ft)-high shaft surrounded by seven 45-m-(148-ft)-high caissons. The caissons (or cells) each have an inner diameter of 33.9 m (111 ft). The shaft has an inner diameter of 43.4 m (142 ft) near the base and begins to taper, at an elevation of 70 m (230 ft), to a minimum of 30.0 m (98.4 ft) near the top of the structure.

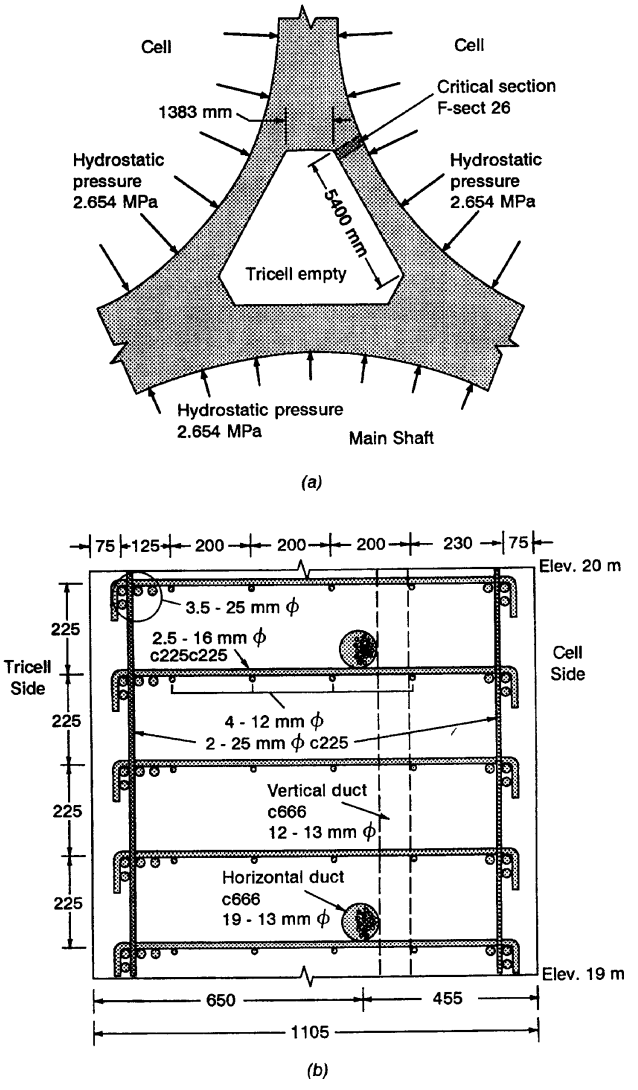

Fig. 10—Draugen GBS: (a) tricell configuration; (b) reinforcing details

The Draugen tricell differs from the Sleipner tricell in several ways. The tricell void is closed in the Draugen design so water pressure is not exerted on the inner part of the wall [Fig. 10(a)]. Also, the caissons are open to the external water pressure. The effect of these changes is that the net pressure on the tricell walls acts in the opposite direction than in the Sleipner platform. The caisson side of the tricell wall was curved with a radius of 16.95 m (55.6 ft), but the inner part of the tricell wall was straight and spanned 5.4 m (17.7 ft). The wall thickness ranged from 900 mm (35.4 in.) at the midspan to 1105 mm (43.5 in.) near the throat of the tricell (i.e., F-Sect 26).

The area of prime concern was F-Sect 26, located at an elevation of 20.18 m (66.2 ft). At this section, the orthogonal grid of steel at the tricell side of the wall consisted of three and one-half 25-mm (1-in.) bars spaced 225 mm (8.9 in.) apart for the horizontal reinforcement, and two 25-mm (1-in.) bars spaced 225 mm (8.9 in.) apart for the vertical reinforcement [Fig. 10(b)]. At the caisson side of the wall, the vertical steel was the same but the horizontal steel was reduced to three 25-mm (1-in.) bars spaced at 225 mm (8.9 in.). Vertical and horizontal post-tensioning was also used in this struc-

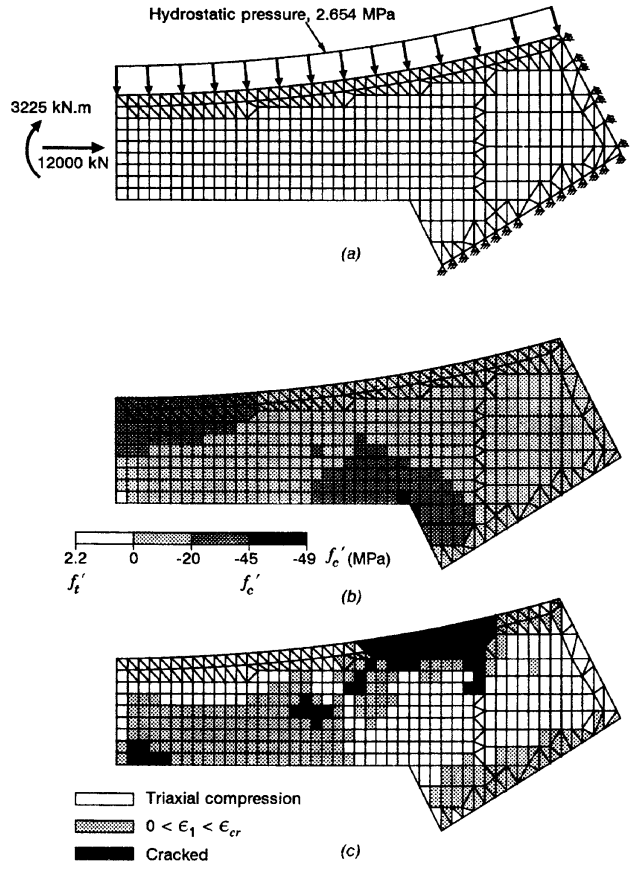

Fig. 11—Analysis of Draugen tricell: (a) finite element mesh; (b) variation of principal compressive stresses; (c) variation of principal tensile strains

ture. Shear reinforcement was also provided in the tricell walls near the throat of the joint. The out-of-plane reinforcement consisted of two and one-half 16-mm (0.63-in.) bars spaced at 225 mm (8.9 in.) vertically and 225 mm (8.9 in.) horizontally to give a reinforcement ratio of 0.993 percent. In addition, two 25-mm (1-in.) "handlebars" spaced 225 mm (8.9 in.) vertically, and 12-mm (0.5-in.) bars spaced 900 mm (35.4 in.) horizontally and 225 mm (8.9 in.) vertically, were placed in the throat of the tricell.

Since the analysis was required to serve as a documentation of design capacity, material and load coefficients were implemented in accordance with the Norwegian standards NS 3473 (1989). The detail design of the Draugen platform was based on a normal density concrete with a cube strength of 70 MPa (10.1 ksi). A usable design strength of 45.0 MPa (6.52 ksi) was calculated after all the code material factors were applied. Additional concrete properties included an initial concrete modulus of elasticity of 36,000 MPa (5220 ksi) and an initial Poisson's ratio of 0.15. For the non-prestressed reinforcement, the design yield stress was 435 MPa (63 ksi) and Young's modulus was 200,000 MPa (29,000 ksi). The prestressed reinforcement had a design yield stress of 1450 MPa (210 ksi) and a Young's modulus of 195,000 MPa (28,300 ksi).

Again, only one-sixth of the tricell region was modeled because of the symmetry. The finite element mesh used to model a 1-m (3.3- ft) height of the tricell wall is shown in Fig. 11(a). The mesh consisted of 329 brick elements and 237 wedge elements. In addition, truss elements were used to model the curved longitudinal reinforcement along the outer part of the tricell wall and the curved longitudinal prestressed reinforcement.

A hydrostatic pressure of 2.654 MPa (385 psi) was applied as equivalent nodal forces along the curved boundary of the tricell. Note that for Sleipner, the net hydrostatic pressure was applied along the inner part of the tricell wall (i.e., in the opposite direction). To produce the correct forces at the critical section (F-Sect 26), an axial force of 11,400 kN/m (780 kip/ft) and a moment of 3225 kN-m/m (725 kip-ft/ft) were applied at the midspan of the tricell wall. The moment and shear at F-Sect 26 were 6082 kN-m/m and 7240 kN/m (1367 kip-ft/ft and 496 kip/ft), respectively. The axial force was assumed to be uniformly distributed across the tricell wall and the moment was treated as linearly varying stresses across the tricell wall. These stresses were then converted to equivalent nodal loads and applied to the finite element model. The prestressing forces were modeled by specifying an appropriate degree of prestrain (6.0×10^{-3}) in the steel truss elements. The longitudinal prestressed reinforcement and part of the curved caisson side longitudinal nonprestressed reinforcement were modeled discretely with truss elements. All other reinforcement was accounted for in a smeared manner. The mesh was given very strong and stiff properties in the vicinity of the applied axial force and moment to facilitate the transfer of forces. Since the distribution of stresses at this section is unknown, the stiff-end condition eases the transition to the actual pattern of stresses in the composite material.

The initial objective was to determine the behavior of the tricell at the expected loads during the deck-mating. This load condition included a hydrostatic pressure of 2.654 MPa (385 psi), applied axial force of 11,400 kN/m (780 kip/ft), and applied moment of 3225 kN-m/m (725 kip-ft/ft) at the end of the mesh representing the midspan.

The SPARCS analysis found that the tricell was close to failure at this load level. At the "critical section" (F-Sect 26), the concrete at the inner side of the wall was near crushing. In fact, the elements in this region had compressive principal stresses [Fig. 11(b)] in excess of the uniaxial cylinder strength (the SPARCS constitutive model allowed for the beneficial effects of triaxial compression). Much of the shear due to the hydrostatic pressure appeared to be resisted by direct strut action. Low strains were observed in the stirrups near the critical section.

Three regions of cracking could be discerned [Fig. 11(c)]. Flexural cracks were found at midspan at the inner face of the wall and near the critical section along the outer face of the wall. A region of inclined cracks occurred at midheight of the wall, adjacent to the point of termination of the stirrups. The analysis indicated that the wall should remain water-tight.

The ultimate strength of the tricell was also sought. The expected factored loads were all increased proportionately until failure was observed. Capacity was governed by crushing of the concrete at the inner part of the wall near F-Sect 26. Failure occurred at loads 1.15 times higher than the expected factored load level.

The shear problem encountered in the Sleipner tricell did not develop in the Draugen tricell. The shear of the critical section was carried into the throat region by direct compres-

sive stresses. The tricell failed due to crushing of the concrete near the throat at stresses in excess of the uniaxial cylinder strength. The tricell was judged to possess sufficient strength to withstand the loads induced by the submerging for the deck-mating. The Draugen platform was subsequently successfully deck-mated.

CONCLUSIONS

The following conclusions were derived from the studies undertaken:

1) The SPARCS program adequately modeled the response of beam strip specimens subjected to moment, shear, and high axial compression. It adequately quantified the influence of the shear reinforcement.

2) The applications to offshore structures demonstrated the program to be a useful analytical tool. Local nonlinear analysis of a large structure can help determine the adequacy of the design of critical regions.

3) The current empirical code equations used in determining the response of members subject to moment, shear, and axial compression did not perform adequately for any of the structures considered in this paper.[4]

REFERENCES

1. ACI-ASCE Committee 326, "Shear and Diagonal Tension," ACI JOURNAL, *Proceedings* V. 59, No. 1, 1962, pp. 1-30; No. 2, 1962, pp. 277-334; and No. 3, 1962, pp. 351-396.

2. ACI Committee 318, "Building Code Requirements for Reinforced Concrete (ACI 318-89) and Commentary (ACI 318R-89)," American Concrete Institute, Detroit, 1989, 353 pp.

3. Norges Byggstandardiseringsrad (NBR), *Prosjektering av betongkonstruksjoner Beregnings-og konstrukjonsregler (Concrete Structure Design Rules)*, NS 3473, Norges standardiseringsforbund, Oslo, Norway, 1989.

4. Gupta, P. R., "Shear Behavior of Reinforced Concrete Beams Subjected to High Axial Compression," thesis presented to University of Toronto, Toronto, Canada, 1993.

5. Selby, R. G., "Three-Dimensional Constitutive Relations for Reinforced Concrete," thesis presented to University of Toronto, Toronto, Canada, 1993.

6. Vecchio, F. J., and Selby, R. G., "Toward Compression Field Analysis of Reinforced Concrete Solids," *Journal of Structural Engineering*, ASCE, V. 117, No. 6, 1991, pp. 1740- 1758.

7. Vecchio, F. J., and Collins, M. P., "Response of Reinforced Concrete to In-Plane Shear and Normal Stresses," *Publication* No. 82-03, Department of Civil Engineering, University of Toronto, Toronto, Canada, 1982.

8. Vecchio, F. J., and Chan, C. C. L., "Reinforced Concrete Membrane Elements with Perforations," *Journal of Structural Engineering*, ASCE, V. 116, No. 9, 1990, pp. 2344-2360.

9. Hsieh, S. S.; Ting, E. C.; and Chen, W. F., "An Elastic Fracture Model for Concrete," *Proceedings*, Third Engineering Mechanical Division Specifications Conference, ASCE, Austin, Texas, 1979, pp. 437-440.

10. Selby, R. G., and Vecchio, F. J., "Three-Dimensional Constitutive Relations for Reinforced Concrete," *Publication* No. 93-02, Department of Civil Engineering, University of Toronto, Toronto, Canada, 1993.

11. Collins, M. P.; Vecchio, F. J.; and Selby, R. G., "Investigating the Failure of an Offshore Structure," *Concrete International*, 1994. (in press)